ACS APPLIED MATERIALS & INTERFACES

Research Article

Cite This: ACS Appl. Mater. Interfaces 2018, 10, 43570−43577

www.acsami.org

Enhancing CO_2 Adsorption and Separation Properties of Aluminophosphate Zeolites by Isomorphous Heteroatom Substitutions

Yue Yu,[†] Xu Li,[§] Rajamani Krishna,[∥] Yuchuan Liu,[†] Yuanzheng Cui,[†] Jianfeng Du,[†] Zhiqiang Liang,[†] Xiaowei Song,*[,†,⊥] and Jihong Yu*[,†,‡]

[†]State Key Laboratory of Inorganic Synthesis and Preparative Chemistry, College of Chemistry and [‡]International Center of Future Science, Jilin University, 2699 Qianjin Street, Changchun 130012, P. R. China

[§]School of Chemical Engineering & Light Industry, Guangdong University of Technology, Guangzhou 510006, P. R. China

[∥]Van 't Hoff Institute for Molecular Sciences, University of Amsterdam, Science Park 904, Amsterdam 1098 XH, The Netherlands

[⊥]Department of Physical and Macromolecular Chemistry, Faculty of Science, Charles University in Prague, Prague 2 128 43, Czech Republic

Supporting Information

ABSTRACT: Mg, Co-substituted aluminophosphate zeolites with **ERI** framework topology (denoted as MgAPO-ERI and CoAPO-ERI) have been synthesized under hydrothermal conditions by using *N,N,N′,N′*-tetramethyl-1,6-hexanediamine as organic template. Their CO_2 adsorption properties are investigated in comparison to those of the pure aluminophosphate counterpart AlPO-ERI. CoAPO-ERI shows the highest CO_2 uptake of 57.3 $cm^3\ g^{-1}$ (273 K and 1 bar) and the highest isosteric heat of 39.0 kJ mol^{-1} among the three samples. Importantly, the incorporation of Mg^{2+} and Co^{2+} ions in the framework of AlPO-ERI can greatly improve the adsorption selectivities of CO_2 over CH_4 and N_2. Whereafter, transient breakthrough simulations were investigated and further proved the advantages of heteroatoms for separations. These results demonstrate that isomorphous heteroatom substitutions in aluminophosphate zeolites play a key role in enhancing CO_2 adsorption and separation abilities.

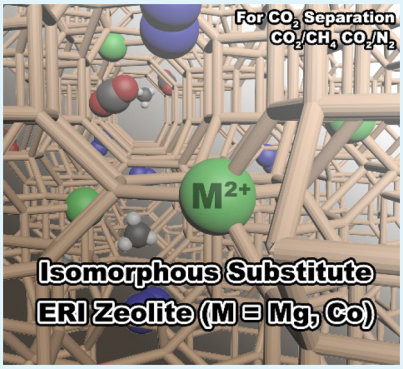

KEYWORDS: *aluminophosphate, **ERI**, heteroatom, isomorphous substitution, CO_2 adsorption*

INTRODUCTION

Global warming and greenhouse effect are seriously undermining the balance of the ecosystem. The benign cycling and effective treatment of carbon dioxide is one of the major concerns of human society. CO_2 capture and sequestration (CCS) process is attracting increasing attention, which provides a transitional solution allowing fossil to be the main energy source for humanity until the maturity of renewable energy technology.[1−3] The most adopted commercialized capture technology is primarily dependent on the adsorption by aqueous amine solutions, which is regenerated by heating under conditions above 100 °C.[4] In such a way, 60−80% cost of the CCS process is spent on the capture and separation steps.[5] The tough problem of large amount of energy cost calls for a low-cost and high-efficiency method to keep pace with the need for low carbon.[3]

The CO_2 selective adsorptions over CH_4 and N_2 are two of the main issues with the deepening of the CCS study, wherein various functional materials, such as zeolites, metal−organic frameworks (MOFs)/zeolitic imidazolate frameworks (ZIFs), carbon composites, and polymers, are widely used.[6−9] High adsorption uptake and selectivity of CO_2 are essential for ideal materials, among which MOFs are potential candidates due to their controllable structures and functions. However, the limited operating condition, low stability, and complicated synthetic procedures hinder their practical applications in the CCS process.[10] Zeolites and some of the stable inorganic open frameworks, which are traditionally used in adsorption, separation, and catalysis, are one of the most promising materials for CCS process because of their diversity in porous structures and chemical functionalities as well as high stabilities in chemical and physical conditions compared to MOFs/ZIFs and others.[11] For a notable example, a microporous copper silicate SGU-29 exhibited a high CO_2 capacity of 156 $cm^3\ cm^{-3}$ (298 K and 1 bar), showing excellent performance in both atmosphere and humid flue gases.[12] Many factors affect the adsorption capacity and selectivity of zeolites for CO_2, such as topologies, channel systems, pore sizes, pore volumes, guest cations, and functional groups.[13−17] Among these, heteroatoms in/out of frameworks are usually beneficial for affinity to

Received: July 5, 2018
Accepted: November 20, 2018
Published: December 4, 2018

DOI: 10.1021/acsami.8b11235
ACS Appl. Mater. Interfaces 2018, 10, 43570−43577

gaseous adsorbates.[18] Currently, ion exchange and isomorphous substitutions are the two common methods of introducing heteroatoms into zeolite materials.[19] Several works have been reported to study the effect of heteroatoms in zeolites through ion exchange on CO_2 adsorption and separation. For instance, Bae et al. evaluated the influence of cation exchange on different topologies of aluminosilicates in postcombustion CO_2 capture.[20] Ke et al. reported a series of high silica RHO zeolites for $CO_2/CH_4/N_2$ separation, in which boron- and copper-containing alkali-metal-crown ether complexes were used as templates.[21] Huong et al. prepared Cu^{2+}- and Fe^{3+}-exchanged zeolites and explored their CO_2 separation over N_2.[22] The above-mentioned results show that heteroatoms would improve both CO_2 adsorption capacity and selectivity. Nonetheless, compared to post-treatment methods in which the heteroatoms occupy the void space of zeolites, framework isomorphous substitutions in zeolites would be a more convenient and straightforward strategy that can maintain more accessible voids for CO_2 adsorption. However, thus far, the influence of heteroatoms introduced by isomorphous substitutions on CO_2 adsorption has rarely been reported.

Aluminophosphate (AlPO) molecular sieves as an important category of zeolites have been extensively studied due to their rich structures ever since their first synthesis in 1982 by Wilson and Flanigen.[23] Subsequent incorporations of silicon and/or metal ions into AlPOs endowed the neutral frameworks with Brønsted acid sites and excellent catalytic and adsorption properties, especially for SAPOs.[15,24] SAPO-34 (CHA) belongs to the ABC-6 zeolite family, whose structures are featured by stacking of three types of six-ring layers in an hexagonal unit cell.[25] It is an outstanding representative of aluminophosphate zeolites that has been used as one of the best industrial catalysts for methanol-to-olefin reactions and is also a potential material for gas adsorption. Previous report showed that SAPO-34 had a good CO_2 adsorption capacity of 3.90 mmol g^{-1} and selectivity over CH_4 of 7.36 at 298 K and 101 kPa.[13] Zhong et al. showed that SAPO-17 (**ERI** topology) membranes displayed a good CO_2/CH_4 selectivity of 53 and CO_2/N_2 selectivity of 14, which were similar to that over SAPO-34 membranes.[26] **ERI**, is also a member of the ABC-6 zeolite family, which has a three-dimensional intersectional 8-ring channel system. The composite building units of *d6r*, can, and elliptic cages of $[4^{12}6^{5}8^{6}]$ constitute the 8-ring pores (3.6 × 5.1 Å). Interestingly, AlPO-17 is one of the best reported materials for pure aluminophosphates in CO_2 adsorption amount (2.5 mmol g^{-1}, 273 K, and 100 kPa).[27] Here, in this study, we have for the first time introduced heteroatoms in **ERI** aluminophosphate zeolites by isomorphous framework substitutions to boost the CO_2 adsorption and separation properties. Heteroatom-containing aluminophosphate zeolites with **ERI** topology MAPO-ERI (M = Mg^{2+}, Co^{2+}) are synthesized under hydrothermal conditions. Studies on the CO_2 adsorption and separation of MAPO-ERI demonstrate that the introduction of heteroatoms through isomorphous framework substitutions could greatly improve the CO_2 adsorption and separation abilities. This work will provide a useful guidance for the design of highly efficient zeolite materials for potential CCS applications.

EXPERIMENTAL SECTION

Materials. All the reagents were obtained from commercial sources and used without purification. Aluminum isopropoxide (≥98% purity) were obtained from Tianjin Guangfu Fine Chemical Research Institute. H_3PO_4 (85 wt %) was supplied by the Beijing Chemical Reagent Factory. $Mg(OAc)_2{\cdot}4H_2O$ or $Co(NO_3)_2{\cdot}6H_2O$ was obtained from Sinopharm Chemical Reagent Co., Ltd. *N,N,N′,N′*-Tetramethyl-1,6-hexanediamine (TMHDA) were obtained from Aladdin Chemical Reagent Co.

Synthesis of AlPO-ERI. In a typical synthesis, 0.408 g $Al(^{i}PrO)_3$ was dispersed in a solution of 7 mL H_2O and 0.307 g H_3PO_4 (85 wt % in water). Then, 0.200 mL TMHDA was stirred into the mixture. A homogeneous gel would form with a molar composition of 1.00 $Al(^{i}PrO)_3$: 1.33 H_3PO_4: 0.47 TMHDA: 200.00 H_2O. The gel would then be stirred for another half an hour. The hydrothermal synthesis condition was set at 453 K for 2 days in 23 mL Teflon-lined stainless-steel autoclaves. The white crystals could be obtained after separation by filtration with continuous washing. Following characterizations would then be performed for the sample after drying at 333 K over night.

Synthesis of MgAPO-ERI and CoAPO-ERI. In a similar way, 0.368 g $Al(^{i}PrO)_3$ was dispersed in a solution of 7 mL H_2O and 0.383 g H_3PO_4 (85 wt % in water). Then, 0.044 g $Mg(OAc)_2{\cdot}4H_2O$ or 0.058 g $Co(NO_3)_2{\cdot}6H_2O$ was added into the solution, followed by the addition of 0.570 mL TMHDA using pipettes. A homogeneous gel would form with a molar composition of 0.10 MO: 0.90 $Al(^{i}PrO)_3$: 1.67 H_3PO_4: 1.33 TMHDA: 200.00 H_2O. The following steps are same as those for AlPO-ERI, with the only difference of a lower crystallization temperature of 443 K.

Characterization. Powder X-ray diffraction was recorded on a Rigaku D/max-2550 diffractometer with a Cu Kα radiation (λ = 1.5418 Å). The inductively coupled plasma atomic emission spectra (ICP-AES) analyses were performed on a PerkinElmer Optima 3300DV spectrometer. Nitrogen (N_2), carbon dioxide (CO_2), and methane (CH_4) sorption experiments were performed on Micromeritics ASAP 2020 instrument, and the temperatures were controlled by condensation pump and Dewar flask with the fluctuations less than ±0.2 K during the experiment.

RESULTS AND DISCUSSION

Syntheses and Characterizations. AlPO-ERI was hydrothermally synthesized in the gel with a molar composition of 1.0 Al_2O_3: 1.33 P_2O_5: 0.94 TMHDA: 400 H_2O and MgAPO-ERI and CoAPO-ERI were hydrothermally synthesized in the gel mixtures with molar composition 0.1MO: 0.45 Al_2O_3: 1.67 P_2O_5: 2.33 TMHDA: 200 H_2O (M = Mg, Co). It could be confirmed that the samples are pure phases by their consistent powder X-ray diffraction patterns with the simulated one of **ERI** (Figure 1). Their scanning electron microscopy (SEM) images display a rodlike morphology (Figure S1). Inductively coupled plasma atomic emission spectra (ICP-AES) analyses

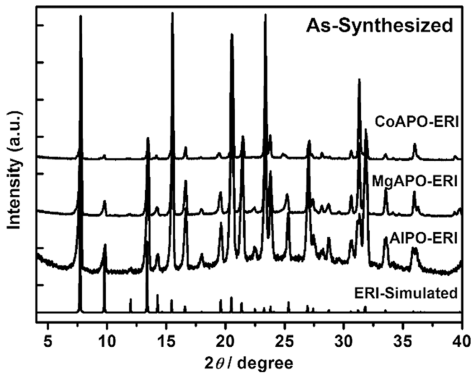

Figure 1. Experimental powder X-ray diffraction patterns of the as-synthesized AlPO-ERI, MgAPO-ERI, CoAPO-ERI, and their simulated one.

DOI: 10.1021/acsami.8b11235
ACS Appl. Mater. Interfaces 2018, 10, 43570−43577

gave the Mg and Co molar contents of MgAPO-ERI and CoAPO-ERI of 8.7 and 13.9%, respectively (Table S1). The elemental mapping images shows that the heteroatoms are uniformly distributed rather aggregated together (Figure S2).

Thermal and hydrothermal stabilities of these three samples were tested. After heating at 550 °C for 6 h, the structures of the three samples can be maintained (Figure S3). The hydrothermal stability was studied by steaming the samples in vapor at 110 °C for 2, 5, and 10 h. Figure S4 shows that MgAPO-ERI is more stable than CoAPO-ERI after the steaming treatment. The structure of MgAPO-ERI was kept stable upon treatment for 10 h, whereas CoAPO-ERI collapsed upon treatment for 5 h.

N_2 adsorption isotherms were measured at 77 K to study the texture properties of the **ERI** samples. As shown in Figure 2, all of them exhibit classic type I isotherms according to IUPAC classification. The Brunauer–Emmett–Teller (BET) specific surface areas could be calculated to be 581 $m^2 g^{-1}$ for AlPO-ERI, 494 $m^2 g^{-1}$ for MgAPO-ERI, and 535 $m^2 g^{-1}$ for CoAPO-ERI (Table 1). Micropore volumes of AlPO-ERI, MgAPO-ERI, and CoAPO-ERI are 0.22, 0.17, and 0.19 $cm^3 g^{-1}$ by the t-plot model, respectively. Pore-size distributions are calculated by the density functional theory (DFT) model, giving 0.63 nm for AlPO-ERI, 0.59 nm for MgAPO-ERI, and 0.63 nm for CoAPO-ERI.

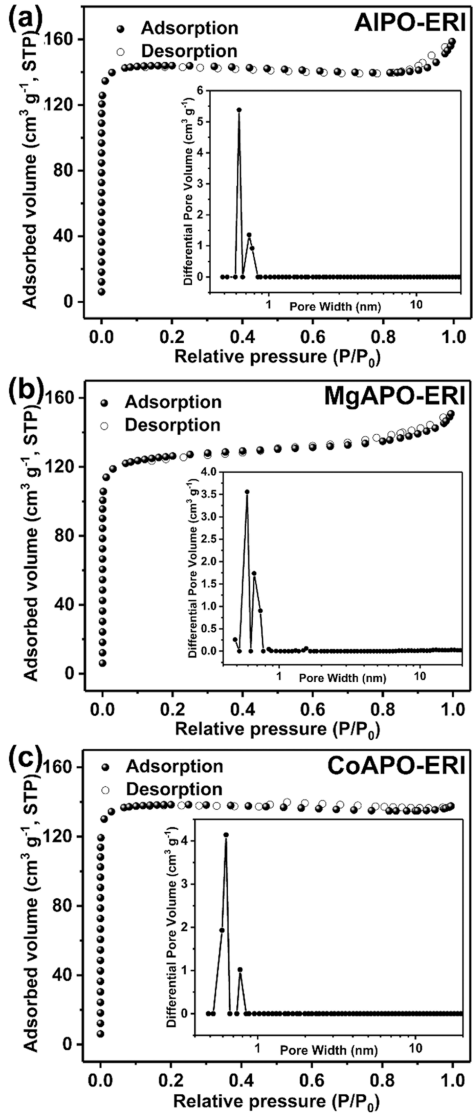

Figure 2. N_2 adsorption and desorption isotherms and pore-size distributions (insets) of calcined AlPO-ERI (a), MgAPO-ERI (b), and CoAPO-ERI (c) at 77 K.

CO_2 Adsorption. CO_2 adsorption isotherms of the three samples were measured at 273, 283, and 298 K, respectively (Figure 3 and Table 1). As can be seen, their adsorption quantities decrease with increase in temperature. In the low-pressure area below 0.1 bar, the uptake of CO_2 is in the order of CoAPO-ERI > MgAPO-ERI > AlPO-ERI (Figure S5 and Table S2). In the high-pressure area, CoAPO-ERI displays the highest uptakes of CO_2 at different temperatures. And the uptakes of CO_2 keep the order of CoAPO-ERI (35.3 $cm^3 g^{-1}$) > MgAPO-ERI (31.7 $cm^3 g^{-1}$) > AlPO-ERI (31.6 $cm^3 g^{-1}$) at 298 K and 1 bar. These results clearly show that the heteroatom substitutions can promote the CO_2 adsorption capacity of **ERI**. Notice that at 273 and 283 K and 1 bar, the CO_2 uptake of MgAPO-ERI are lower than those of AlPO-ERI, which might be due to the relatively lower pore volume of MgAPO-ERI. Compared with other pure aluminophosphate zeolites, CoAPO-ERI (57.3 $cm^3 g^{-1}$) appears to be one of the best materials for CO_2 adsorption (Table S3), which is only inferior to AlPO-14 (AFN, 60.6 $cm^3 g^{-1}$ at 273 K and 100 kPa).[28] Even at higher temperature (298 K), isomorphous-substituted zeolites show obvious higher CO_2 capacities after introducing heteroatoms. This is different from several reported cation-exchanged zeolites in which the voids of zeolites are occupied by the exchanged cations leading to the decrease in CO_2 uptake.[29] Isomorphous substitution in aluminophosphates is noteworthy in that it results in the electroneutral framework active sites that are uncapable of cation exchange.

To better investigate the relationship between CO_2 adsorption properties and heteroatom substitutions in ERI, the isosteric heats of CO_2 adsorption (Q_{st}) for AlPO-ERI, MgAPO-ERI, and CoAPO-ERI were calculated by fitting the CO_2 adsorption isotherms at 273, 283, and 298 K to the virial equation. As shown in Table 1 and Figure 3d, the Q_{st} for CoAPO-ERI (39.0 kJ mol^{-1}) is the highest, which is much higher than that of MgAPO-ERI (33.5 kJ mol^{-1}) and AlPO-ERI (20.4 kJ mol^{-1}). This result indicates that the transition element Co could greatly enhance the interaction between CO_2 adsorbate and the inorganic framework compared with the main group element Mg. This could be attributed to the d-orbital of the transition element, which might form the d–π coordination and increase the affinity between the framework and the CO_2 molecules, thus having a more obvious effect than the main group element.[22,30,31] Therefore, in the low-quantity-adsorbed area, CoAPO-ERI is advantageous for the capture of CO_2 molecules due to its high Q_{st}. In the high-quantity-adsorbed area, the Q_{st} values of the three samples are almost the same after the consumption of metal sites, indicating the sorption behaviors are mainly determined by the frameworks.[32] These results are in the same range as those for some of the inorganic porous materials, such as Silicate-1 (20 kJ mol^{-1}), AlPO-14 (35.2 kJ mol^{-1}), AlPO-5 (15 kJ mol^{-1}), SAPO-5 (22 kJ mol^{-1}), SAPO-56 (32 kJ mol^{-1}), and SAPO-RHO (32 kJ mol^{-1}), which is in the physisorption range (20–50 kJ mol^{-1}).[24,28,33−35]

Selective Adsorption Properties of CO_2 over N_2 and CH_4 and Breakthrough Simulations. To investigate the influences of heteroatoms on the CO_2 adsorption selectivities

DOI: 10.1021/acsami.8b11235
ACS Appl. Mater. Interfaces 2018, 10, 43570−43577

Table 1. Porosity Properties, CO_2, Q_{st}, CO_2, CH_4, and N_2 Adsorption Quantities of AlPO-ERI, MgAPO-ERI, and CoAPO-ERI at 1 bar at Different Temperatures (K)

				CO_2 (cm^3 g^{-1})			CH_4 (cm^3 g^{-1})		N_2 (cm^3 g^{-1})
sample	pore volume (cm^3 g^{-1})	BET surface area (m^2 g^{-1})	Q_{st} (kJ mol^{-1})	273	283	298	273	298	273
AlPO-ERI	0.22	581	20.4	52.5	45.7	31.6	18.4	9.0	4.3
MgAPO-ERI	0.17	494	33.5	49.4	43.9	31.7	16.9	8.6	5.0
CoAPO-ERI	0.19	535	39.0	57.3	47.8	35.3	18.4	9.2	6.0

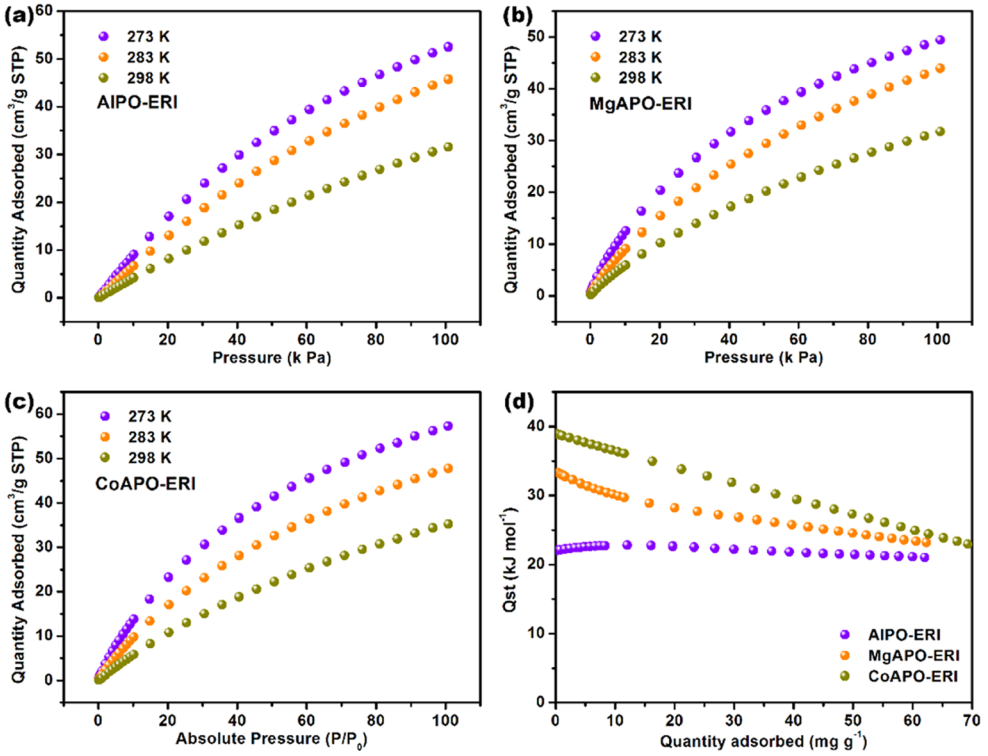

Figure 3. CO_2 adsorption of AlPO-ERI (a), MgAPO-ERI (b), and CoAPO-ERI (c) at 273, 283, and 298 K. (d) The isosteric heat of adsorption (Q_{st}) for AlPO-ERI, MgAPO-ERI, and CoAPO-ERI.

over N_2 and CH_4, the adsorption isotherms of N_2 (273 K) and CH_4 (273 and 298 K) of AlPO-ERI, MgAPO-ERI, and CoAPO-ERI were measured (Figure 4a–c). The adsorption capacities are in the order of CO_2 > CH_4 > N_2 for each sample, indicating the preferential adsorption for CO_2 over both CH_4 and N_2. The CO_2 selectivities of the two different binary gases of CO_2/N_2 (0.5:0.5 and 0.15:0.85) and CO_2/CH_4 (0.5:0.5 and 0.05:0.95) at 100 kPa were predicted by ideal adsorbed solution theory (IAST). The adsorption isotherms were well fitted by dual-site Langmuir–Freundlich adsorption model (R^2 > 0.999). The fitting parameters were then used to predict the multicomponent adsorption with IAST.

As shown in Figure 4d–f, MgAPO-ERI and CoAPO-ERI show much higher selectivities for CO_2/N_2 than AlPO-ERI within the low-pressure range. Particularly, the selectivity of MgAPO-ERI is much higher than that of CoAPO-ERI when the pressure is around zero. With the increase in pressure, the selectivities decrease gradually to attain a balance. At 100 kPa and 273 K, MgAPO-ERI shows the highest CO_2/N_2 selectivities of 28.49 (0.5:0.5) and 29.41 (0.15:0.85), whereas CoAPO-ERI shows relatively lower selectivities of 24.63 (0.5:0.5) and 27.24 (0.15:0.85) (Table 2). By contrast, AlPO-ERI shows the lowest selectivities of 18.20 (0.5:0.5) and 17.57 (0.15:0.85). It is obvious that the substitutions of Mg^{2+} and Co^{2+} ions could greatly improve the adsorption selectivity of CO_2/N_2 for AlPO-ERI.

For selective adsorption of CO_2 over CH_4, both MgAPO-ERI and CoAPO-ERI show a better performance than AlPO-ERI, and the selectivities of CO_2/CH_4 decrease with increase in pressure (Figure 4d–f). Notably, MgAPO-ERI shows the highest selectivity of 7.26 (0.5:0.5) and 7.90 (0.05:0.95) at 100 kPa and 273 K (Table 2). At 100 kPa and 298 K, MgAPO-ERI also exhibits the highest selectivity of 6.77 (0.5:0.5) and 6.66 (0.05:0.95).

For the selectivities of both CO_2/CH_4 and CO_2/N_2, raw MgAPO-ERI shows performances comparable to those of other types of zeolites and better ones than some of the MOFs materials.[28,29,36−47] To verify the superiority of heteroatoms, Henry's law is used to calculate the selectivities for CO_2/CH_4 and CO_2/N_2 at 273 K and for CO_2/CH_4 at 298 K (Figure S6 and Table 3). As can be seen, MgAPO-ERI always has the highest selectivity in these conditions, which is in accordance with the IAST calculations.

The separation performances of AlPO-ERI, MgAPO-ERI, and CoAPO-ERI in fixed-bed adsorbers were investigated using transient breakthrough simulation; the simulation methodology is described in earlier publications.[48−51] The breakthroughs were carried out for (1) $CO_2/CH_4/N_2$ gaseous mixtures with equimolar ratio operating at 100 kPa and 273 K

DOI: 10.1021/acsami.8b11235
ACS Appl. Mater. Interfaces 2018, 10, 43570−43577

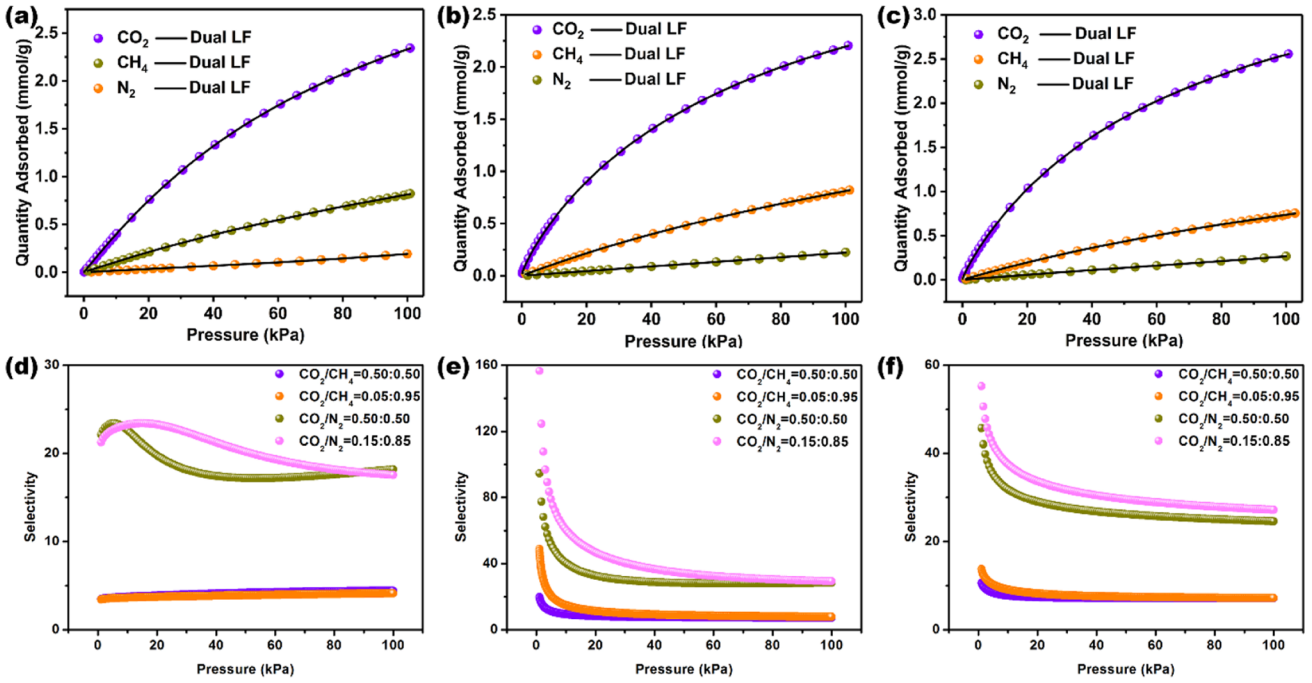

Figure 4. CO_2, CH_4, and N_2 gas adsorption isotherms for AlPO-ERI (a), MgAPO-ERI (b), and CoAPO-ERI (c) at 273 K. CO_2/CH_4 and CO_2/N_2 IAST selectivity for AlPO-ERI (d), MgAPO-ERI (e), and CoAPO-ERI (f) at 273 K.

Table 2. CO_2/CH_4 and CO_2/N_2 IAST Separation of AlPO-ERI, MgAPO-ERI, and CoAPO-ERI at 273 and 298 K and 1 bar

	CO_2/CH_4 at 273 K		CO_2/CH_4 at 298 K		CO_2/N_2 at 273 K	
sample	0.50:0.50	0.05:0.95	0.50:0.50	0.05:0.95	0.50:0.50	0.15:0.85
AlPO-ERI	4.43	4.15	4.49	3.91	18.20	17.57
MgAPO-ERI	7.26	7.90	6.77	6.66	28.49	29.41
CoAPO-ERI	7.17	7.22	5.87	5.48	24.63	27.24

Table 3. CO_2 Selectivities by Henry's Law

	$K_H(CO_2)/K_H(CH_4)$ at 273 K	$K_H(CO_2)/K_H(CH_4)$ at 298 K	$K_H(CO_2)/K_H(N_2)$ at 273 K
AlPO-ERI	3.94	3.47	23.65
MgAPO-ERI	8.53	6.42	36.95
CoAPO-ERI	8.19	4.8	30.16

and (2) equimolar CO_2/CH_4 gaseous mixtures with equimolar ratio operating at 100 kPa and 298 K. As shown in Figure 5, the breakthrough time is of the order of $CO_2 > CH_4 > N_2$ for each of the samples, which is in line with the adsorption capacities. On the basis of the transient breakthrough simulations, metal-substitution obviously improved the performance of AlPO-ERI, where the best separation performance for both mixtures is achieved over CoAPO-ERI in the fixed-bed adsorber, which could be attributed to its significantly higher carbon dioxide uptake capacity.[48,51]

Generally, the CO_2 adsorption and separation could be related to several issues such as Q_{st}, pore sizes, capacities, structures, etc. Several DFT calculations have adopted periodic models to study the adsorption on zeolites.[52−54] For example, Chatterjee investigated metal substituents from a range of metal cation on the acidic property (both Brønsted and Lewis) of MAPOs.[55] In this work, the FTIR spectra after pyridine adsorption show that both Brønsted (1545 cm^{-1}) and Lewis (1450 cm^{-1}) acid sites exist in ERI aluminophosphate zeolites (Figure S7). Besides, the XPS spectrum of Co 2p confirms the existence of Co^{3+} (Figure S8), which would give out Lewis acid sites. It is considered that the interactions are related to both strength and concentration of Brønsted and Lewis acid sites in AlPI-ERI, MgAPO-ERI, and CoAPO-ERI.

CONCLUSIONS

In summary, aluminophosphate zeolites with **ERI** topology including AlPO-ERI, MgAPO-ERI, and CoAPO-ERI were synthesized and their CO_2 adsorption properties investigated. The incorporation of heteroatoms can remarkably improve the isosteric heat of adsorption of CO_2 of **ERI**; particularly, CoAPO-ERI showed the highest Q_{st} of 39.0 kJ mol^{-1}. Consequently, CoAPO-ERI showed the highest CO_2 adsorption capacity of 57.3 cm^3 g^{-1} (273 K and 1 bar), which is among the highest values for pure aluminophosphate zeolites. Meanwhile, an enhancement in the selectivities of CO_2/CH_4 and CO_2/N_2 was also observed for MAPO-ERI, among which MgAPO-ERI showed a more obvious effect than CoAPO-ERI. Transient breakthrough simulations also proved the advantages of heteroatoms for separations. This work demonstrates an effective way to improve the CO_2 adsorption properties of aluminophosphate zeolites by isomorphous substitutions.

DOI: 10.1021/acsami.8b11235
ACS Appl. Mater. Interfaces 2018, 10, 43570−43577

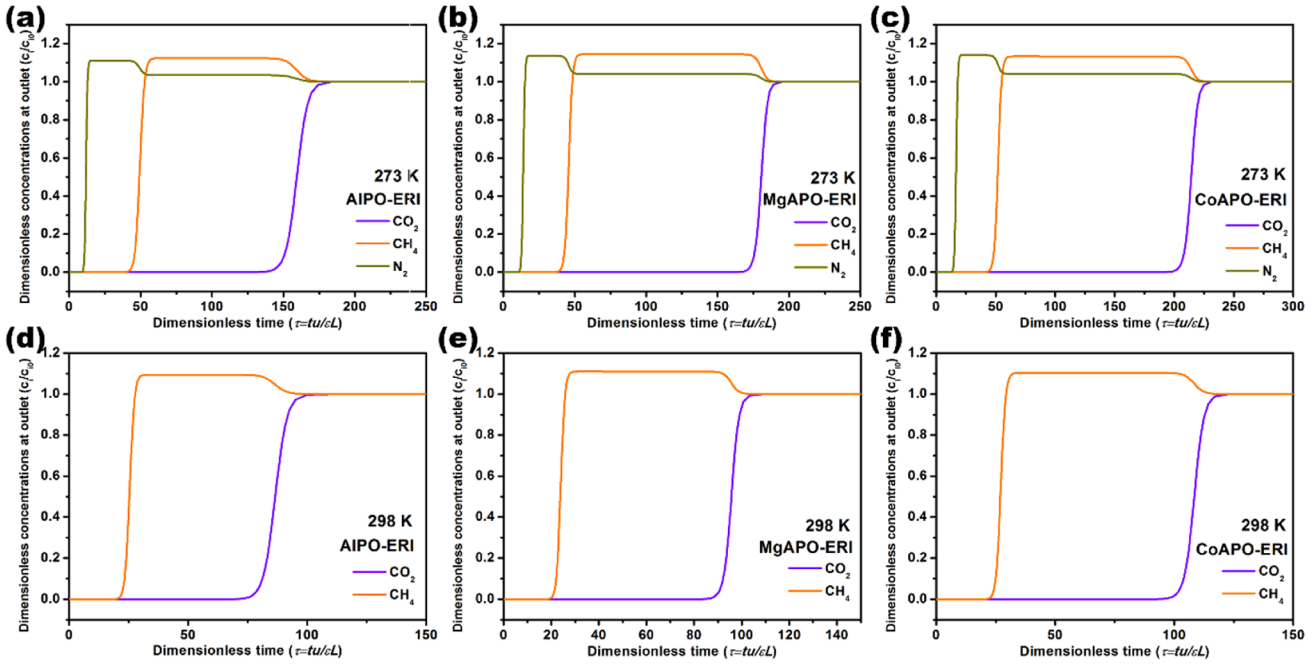

Figure 5. Transient breakthrough simulation data for equimolar three-component $CO_2/CH_4/N_2$ mixture at 100 kPa and 273 K of AlPO-ERI (a), MgAPO-ERI (b), and CoAPO-ERI (c) and for equimolar two-component CO_2/CH_4 mixture at 100 kPa and 273 K of AlPO-ERI (d), MgAPO-ERI (e), and CoAPO-ERI (f).

Moreover, it provides an insight into the understanding of the CO_2 adsorption influenced by heteroatoms and the acidity of zeolites, which will be useful for the design of highly efficient zeolite materials for CO_2 capture and separation.

■ ASSOCIATED CONTENT

Supporting Information

The Supporting Information is available free of charge on the ACS Publications website at DOI: 10.1021/acsami.8b11235.

Calculations of the isosteric heats of gas adsorption (Q_{st}); prediction of adsorption of binary mixture by IAST theory; transient breakthrough of mixtures in fixed-bed adsorbers; SEM images of the samples and element distributions; XRD patterns of stabilities; elemental analysis; virial fittings of CO_2 isotherms; fitting patterns and parameters of DSLF adsorption model and Henry's law; CO_2 adsorptions and separations at 298 K; reported CO_2 adsorption properties for comparison; XPS spectra; IR spectra after adsorption of pyridine (PDF)

■ AUTHOR INFORMATION

Corresponding Authors

*E-mail: xiaoweisong@jlu.edu.cn (X.S.).
*E-mail: jihong@jlu.edu.cn (J.Y.).

ORCID

Yue Yu: 0000-0002-8189-8291
Rajamani Krishna: 0000-0002-4784-8530
Zhiqiang Liang: 0000-0003-4473-8544
Xiaowei Song: 0000-0002-1007-4965
Jihong Yu: 0000-0003-1615-5034

Notes

The authors declare no competing financial interest.

■ ACKNOWLEDGMENTS

We thank the National Key Research and Development Program of China (Grant 2016YFB0701100), the National Natural Science Foundation of China (Grants 21835002, 21621001, and 21871104), the 111 project (Grant B17020) and OP VVV "Excellent Research Teams" (Grant CZ.02.1.01/0.0/0.0/15_003/0000417-CUCAM) for this work.

■ REFERENCES

(1) Patel, H. A.; Byun, J.; Yavuz, C. T. Carbon Dioxide Capture Adsorbents: Chemistry and Methods. *ChemSusChem* **2017**, *10*, 1303−1317.

(2) Wang, W.; Zhou, M.; Yuan, D. Carbon Dioxide Capture in Amorphous Porous Organic Polymers. *J. Mater. Chem. A* **2017**, *5*, 1334−1347.

(3) Bae, Y.-S.; Snurr, R. Q. Development and Evaluation of Porous Materials for Carbon Dioxide Separation and Capture. *Angew. Chem., Int. Ed.* **2011**, *50*, 11586−11596.

(4) Chaffee, A. L.; Knowles, G. P.; Liang, Z.; Zhang, J.; Xiao, P.; Webley, P. A. CO_2 Capture by Adsorption: Materials and Process Development. *Int. J. Greenhouse Gas Control* **2007**, *1*, 11−18.

(5) Liu, Q.; Cheung, N. C. O.; Garcia-Bennett, A. E.; Hedin, N. Aluminophosphates for CO_2 Separation. *ChemSusChem* **2011**, *4*, 91−97.

(6) Yu, J.; Xie, L.-H.; Li, J.-R.; Ma, Y.; Seminario, J. M.; Balbuena, P. B. CO_2 Capture and Separations Using MOFs: Computational and Experimental Studies. *Chem. Rev.* **2017**, *117*, 9674−9754.

(7) Zou, L.; Sun, Y.; Che, S.; Yang, X.; Wang, X.; Bosch, M.; Wang, Q.; Li, H.; Smith, M.; Yuan, S.; Perry, Z.; Zhou, H.-C. Porous Organic Polymers for Post-Combustion Carbon Capture. *Adv. Mater.* **2017**, *29*, No. 1700229.

(8) Yang, X.; Rees, R. J.; Conway, W.; Puxty, G.; Yang, Q.; Winkler, D. A. Computational Modeling and Simulation of CO_2 Capture by Aqueous Amines. *Chem. Rev.* **2017**, *117*, 9524−9593.

(9) Zeng, S.; Zhang, X.; Bai, L.; Zhang, X.; Wang, H.; Wang, J.; Bao, D.; Li, M.; Liu, X.; Zhang, S. Ionic-Liquid-Based CO_2 Capture Systems: Structure, Interaction and Process. *Chem. Rev.* **2017**, *117*, 9625−9673.

DOI: 10.1021/acsami.8b11235
ACS Appl. Mater. Interfaces 2018, 10, 43570−43577

(10) Férey, G. Hybrid Porous Solids: Past, Present, Future. *Chem. Soc. Rev.* **2008**, *37*, 191−214.
(11) Li, Y.; Li, L.; Yu, J. Applications of Zeolites in Sustainable Chemistry. *Chem* **2017**, *3*, 928−949.
(12) Datta, S. J.; Khumnoon, C.; Lee, Z. H.; Moon, W. K.; Docao, S.; Nguyen, T. H.; Hwang, I. C.; Moon, D.; Oleynikov, P.; Terasaki, O.; Yoon, K. B. CO_2 Capture from Humid Flue Gases and Humid Atmosphere Using a Microporous Coppersilicate. *Science* **2015**, *350*, 302−306.
(13) Wang, D.; Tian, P.; Yang, M.; Xu, S.; Fan, D.; Su, X.; Yang, Y.; Wang, C.; Liu, Z. Synthesis of SAPO-34 with Alkanolamines as Novel Templates and Their Application for CO_2 Separation. *Microporous Mesoporous Mater.* **2014**, *194*, 8−14.
(14) Jo, D.; Lim, J. B.; Ryu, T.; Nam, I.-S.; Camblor, M. A.; Hong, S. B. Unseeded Hydroxide-mediated Synthesis and CO_2 Adsorption Properties of an Aluminosilicate Zeolite with the RTH Topology. *J. Mater. Chem. A* **2015**, *3*, 19322−19329.
(15) Bacsik, Z.; Cheung, O.; Vasiliev, P.; Hedin, N. Selective Separation of CO_2 and CH_4 for Biogas Upgrading on Zeolite NaKA and SAPO-56. *Appl. Energy* **2016**, *162*, 613−621.
(16) Zukal, A.; Shamzhy, M.; Kubů, M.; Čejka, J. The Effect of Pore Size Dimensions in Isoreticular Zeolites on Carbon Dioxide Adsorption Heats. *J. CO_2 Util.* **2018**, *24*, 157−163.
(17) Moliner, M.; Martínez, C.; Corma, A. Synthesis Strategies for Preparing Useful Small Pore Zeolites and Zeotypes for Gas Separations and Catalysis. *Chem. Mater.* **2014**, *26*, 246−258.
(18) Li, J.; Corma, A.; Yu, J. Synthesis of New Zeolite Structures. *Chem. Soc. Rev.* **2015**, *44*, 7112−7127.
(19) Hartmann, M.; Kevan, L. Transition-Metal Ions in Aluminophosphate and Silicoaluminophosphate Molecular Sieves: Location, Interaction with Adsorbates and Catalytic Properties. *Chem. Rev.* **1999**, *99*, 635−664.
(20) Bae, T.-H.; Hudson, M. R.; Mason, J. A.; Queen, W. L.; Dutton, J. J.; Sumida, K.; Micklash, K. J.; Kaye, S. S.; Brown, C. M.; Long, J. R. Evaluation of Cation-exchanged Zeolite Adsorbents for Post-Combustion Carbon Dioxide Capture. *Energy Environ. Sci.* **2013**, *6*, 128−138.
(21) Ke, Q.; Sun, T.; Wei, X.; Guo, Y.; Wang, S. Enhanced Trace Carbon Dioxide Capture on Heteroatom-Substituted RHO Zeolites under Humid Conditions. *ChemSusChem* **2017**, *10*, 4207−4214.
(22) Huong, P.-T.; Lee, B.-K. Improvement of Selective Separation of CO_2 over N_2 by Transition Metal-exchanged Nano-zeolite. *Microporous Mesoporous Mater.* **2017**, *241*, 155−164.
(23) Wilson, S. T.; Lok, B. M.; Messina, C. A.; Cannan, T. R.; Flanigen, E. M. Aluminophosphate Molecular Sieves: A New Class of Microporous Crystalline Inorganic Solids. *J. Am. Chem. Soc.* **1982**, *104*, 1146−1147.
(24) Cheung, Q.; Liu, Q.; Bacsik, Z.; Hedin, N. Silicoaluminophosphates as CO_2 Sorbents. *Microporous Mesoporous Mater.* **2012**, *156*, 90−96.
(25) Li, Y.; Li, X.; Liu, J.; Duan, F.; Yu, J. In Silico Prediction and Screening of Modular Crystal Structures via a High-throughput Genomic Approach. *Nat. Commun.* **2015**, *6*, No. 8328.
(26) Zhong, S.; Bu, N.; Zhou, R.; Jin, W.; Yu, M.; Li, S. Aluminophosphate-17 and Silicoaluminophosphate-17 Membranes for CO_2 Separations. *J. Membr. Sci.* **2016**, *520*, 507−514.
(27) Akhtar, F.; Keshavarzi, N.; Shkarova, D.; Cheung, O.; Hedin, N.; Bergström, L. Aluminophosphate Monoliths with High CO_2-over-N_2 Selectivity and CO_2 Capture Capacity. *RSC Adv.* **2014**, *4*, 55877−55883.
(28) Zhao, X.-X.; Xu, X.-L.; Sun, L.-B.; Zhang, L.-L.; Liu, X.-Q. Adsorption Behavior of Carbon Dioxide and Methane on $AlPO_4$-14: A Neutral Molecular Sieve. *Energy Fuels* **2009**, *23*, 1534−1538.
(29) Hudson, M. R.; Queen, W. L.; Mason, J. A.; Fickel, D. W.; Lobo, R. F.; Brown, C. M. Unconventional, Highly Selective CO_2 Adsorption in Zeolite SSZ-13. *J. Am. Chem. Soc.* **2012**, *134*, 1970−1973.
(30) Kim, K.; Lee, T.; Kwon, Y.; Seo, Y.; Song, J.; Park, J. K.; Lee, H.; Park, J. Y.; Ihee, H.; Cho, S. J.; Ryoo, R. Lanthanum-catalysed Synthesis of Microporous 3D Graphene-like Carbons in a Zeolite Template. *Nature* **2016**, *535*, 131−135.
(31) Zhai, Q.-G.; Bu, X.; Mao, C.; Zhao, X.; Feng, P. Systematic and Dramatic Tuning on Gas Sorption Performance in Heterometallic Metal-Organic Frameworks. *J. Am. Chem. Soc.* **2016**, *138*, 2524−2527.
(32) Dietzel, P. D. C.; Besikiotis, V.; Blom, R. Application of Metal-organic Frameworks with Coordinatively Unsaturated Metal Sites in Storage and Separation of Methane and Carbon Dioxide. *J. Mater. Chem.* **2009**, *19*, 7362−7370.
(33) Choudhary, V. R.; Mayadevi, S. Adsorption of Methane, Ethane, Ethylene, and Carbon Dioxide on Silicalite-1. *Zeolites* **1996**, *17*, 501−507.
(34) Choudhary, V. R.; Mayadevi, S. Sorption Isotherms of Methane, Ethane, Ethylene, and Carbon Dioxide on ALPO-5 and SAPO-5. *Langmuir* **1996**, *12*, 980−986.
(35) Amari, D.; Cuesta, J. M. L.; Nguyen, N. P.; Jerrentrup, R.; Ginoux, J. L. Chemisorption and Physisorption of CO_2 on Cation Exchanged Zeolites A, X and MOR. *J. Therm. Anal.* **1992**, *38*, 1005−1015.
(36) Himeno, S.; Tomita, T.; Suzuki, K.; Yoshida, S. Characterization and Selectivity for Methane and Carbon Dioxide Adsorption on the All-silica DD3R Zeolite. *Microporous Mesoporous Mater.* **2007**, *98*, 62−69.
(37) Liu, X.; Li, J.; Zhou, L.; Huang, D.; Zhou, Y. Adsorption of CO_2, CH_4 and N_2 on Ordered Mesoporous Silica Molecular Sieve. *Chem. Phys. Lett.* **2005**, *415*, 198−201.
(38) Palomino, M.; Corma, A.; Rey, F.; Valencia, S. New Insights on CO_2-Methane Separation Using LTA Zeolites with Different Si/Al Ratios and A First Comparison with MOFs. *Langmuir* **2010**, *26*, 1910−1917.
(39) Maghsoudi, H.; Soltanieh, M.; Bozorgzadeh, H.; Mohamadalizadeh, A. Adsorption Isotherms and Ideal Selectivities of Hydrogen Sulfide and Carbon Dioxide over Methane for the Si-CHA Zeolite: Comparison of Carbon Dioxide and Methane Adsorption with the All-silica DD3R Zeolite. *Adsorption* **2013**, *19*, 1045−1053.
(40) Bastin, L.; Bárcia, P. S.; Hurtado, E. J.; Silva, J. A. C.; Rodrigues, A. E.; Chen, B. A Microporous Metal-organic Framework for Separation of CO_2/N_2 and CO_2/CH_4 by Fixed-bed Adsorption. *J. Phys. Chem. C* **2008**, *112*, 1575−1581.
(41) Huang, H.; Zhang, W.; Liu, D.; Liu, B.; Chen, G.; Zhong, C. Effect of Temperature on Gas Adsorption and Separation in ZIF-8: A Combined Experimental and Molecular Simulation Study. *Chem. Eng. Sci.* **2011**, *66*, 6297−6305.
(42) Yang, Q.; Vaesen, S.; Ragon, F.; Wiersum, A. D.; Wu, D.; Lago, A.; Devic, T.; Martineau, C.; Taulelle, F.; Llewellyn, P. L.; Jobic, H.; Zhong, C.; Serre, C.; Weireld, G. D.; Maurin, G. A Water Stable Metal-organic Framework with Optimal Features for CO_2 Capture. *Angew. Chem., Int. Ed.* **2013**, *52*, 10316−10320.
(43) Zhang, J.-W.; Hu, M.-C.; Li, S.-N.; Jiang, Y.-C.; Zhai, Q.-G. Design of Highly Connected Cd-Tetrazolate-Dicarboxylate Frameworks with Enhanced CO_2/CH_4 and C2 Hydrocarbons/CH_4 Separation Performance. *Cryst. Growth Des.* **2016**, *16*, 6430−6435.
(44) Qiao, S.; Du, Z.; Yang, R. Design and Synthesis of Novel Carbazole-spacer-carbazole Type Conjugated Microporous Networks for Gas Storage and Separation. *J. Mater. Chem. A.* **2014**, *2*, 1877−1885.
(45) Belmabkhout, Y.; Sayari, A. Adsorption of CO_2 from Dry Gases on MCM-41 Silica at Ambient Temperature and High Pressure. 2: Adsorption of CO_2/N_2, CO_2/CH_4 and CO_2/H_2 Binary Mixtures. *Chem. Eng. Sci.* **2009**, *64*, 3729−3735.
(46) Zukal, A.; Pawlesa, J.; Čejka, J. Isosteric Heats of Adsorption of Carbon Dioxide on Zeolite MCM-22 Modified by Alkali Metal Cations. *Adsorption* **2009**, *15*, 264−270.
(47) Zukal, A.; Mayerová, J.; Čejka, J. Alkali Metal Cation Doped Al-SBA-15 for Carbon Dioxide Adsorption. *Phys. Chem. Chem. Phys.* **2010**, *12*, 5240−5247.

DOI: 10.1021/acsami.8b11235
ACS Appl. Mater. Interfaces 2018, 10, 43570−43577

(48) Krishna, R. The Maxwell-Stefan Description of Mixture Diffusion in Nanoporous Crystalline Materials. *Microporous Mesoporous Mater.* **2014**, *185*, 30−50.
(49) Krishna, R. Methodologies for Evaluation of Metal-Organic Frameworks in Separation Applications. *RSC Adv.* **2015**, *5*, 52269−52295.
(50) Krishna, R. Screening Metal-Organic Frameworks for Mixture Separations in Fixed-Bed Adsorbers using a Combined Selectivity/Capacity Metric. *RSC Adv.* **2017**, *7*, 35724−35737.
(51) Krishna, R. Methodologies for Screening and Selection of Crystalline Microporous Materials in Mixture Separations. *Sep. Purif. Technol.* **2018**, *194*, 281−300.
(52) Potter, M. E.; Paterson, A. J.; Mishra, B.; Kelly, S. D.; Bare, S. R.; Cora, F.; Levy, A. B.; Raja, R. Spectroscopic and Computational Insights on Catalytic Synergy in Bimetallic Aluminophosphate Catalysts. *J. Am. Chem. Soc.* **2015**, *137*, 8534−8540.
(53) Nachtigall, P.; Grajciar, L.; Pérez-Pariente, J.; Pinar, A. B.; Zukal, A.; Čejka, J. Control of CO_2 Adsorption Heats by the Al Distribution in FER Zeolites. *Phys. Chem. Chem. Phys.* **2012**, *14*, 1117−1120.
(54) Pulido, A.; Delgado, M. R.; Bludský, O.; Rubeš, M.; Nachtigall, P.; Areán, C. O. Combined DFT/CC and IR Spectroscopic Studies on Carbon Dioxide Adsorption on the Zeolite H-FER. *Energy Environ. Sci.* **2009**, *2*, 1187−1195.
(55) Chatterjee, A. A Reactivity Index Study to Rationalize the Effect of Dopants on Brønsted and Lewis Acidity Occurring in MeAlPOs. *J. Mol. Graphics Modell.* **2006**, *24*, 262−270.

DOI: 10.1021/acsami.8b11235
ACS Appl. Mater. Interfaces 2018, 10, 43570−43577

Supporting Information

Enhancing CO_2 Adsorption and Separation Properties of Aluminophosphate Zeolites by Isomorphous Heteroatom Substitutions

Yue Yu[†], *Xu Li*[§], *Rajamani Krishna*[//], *Yuchuan Liu*[†], *Yuanzheng Cui*[†], *Jianfeng Du*[†], *Zhiqiang Liang*[†], *Xiaowei Song*[*,†,⊥], *Jihong Yu*[**,†,‡]

[†]State Key Laboratory of Inorganic Synthesis and Preparative Chemistry, College of Chemistry and [‡]International Center of Future Science, Jilin University, 2699 Qianjin Street, Changchun 130012, P. R. China

[§] School of Chemical Engineering & Light Industry, Guangdong University of Technology, Guangzhou 510006, P. R. China

[//]Van 't Hoff Institute for Molecular Sciences, University of Amsterdam, Science Park 904, Amsterdam 1098 XH, The Netherlands

[⊥]Department of Physical and Macromolecular Chemistry, Faculty of Science, Charles University in Prague, Prague 2 128 43, Czech Republic

Corresponding Author

* E-mail: xiaoweisong@jlu.edu.cn.

** E-mail: jihong@jlu.edu.cn.

Experimental

Calculations of the Isosteric Heats of Gas Adsorption (*Q*st):

The isosteric heats (Q_{st}) of adsorption for AlPO-ERI, MgAPO-ERI and CoAPO-ERI were calculated by fitting the CO_2 adsorption isotherms measured at 263 K, 273 K, 283 K and 298 K to the Virial equation. [1]

$$\ln P = \ln N + {}^{1}/_{T} \sum_{i=0}^{m} a_i N^i + \sum_{j=0}^{n} b_j N^j \qquad (1)$$

$$Q_{st} = -R \sum_{i=0}^{m} a_i N^i \qquad (2)$$

N: amount adsorbed (mg/g);

P: pressure (mmHg);

T: temperature (K);

a_i, b_j: constants;

R: 8.314 J mol^{-1} K^{-1}

Prediction of adsorption of binary mixture by IAST theory

In order to perform the IAST calculations, the single-component isotherm was fitted by the dual-site Langmuir-Freundlich (DSLF) adsorption model to correlate the pure-component equilibrium data and further to predict the adsorption of mixtures.[2] The DSLF model is described as:

$$q = q_{m_1} \times \frac{b_1 \times p^{1/n_1}}{1 + b_1 \times p^{1/n_1}} + q_{m_2} \times \frac{b_2 \times p^{1/n_2}}{1 + b_1 \times p^{1/n_2}} \qquad (3)$$

Where p is the fugacity of bulk gas at equilibrium with adsorbed phase, q_{m1} and q_{m2} are the model parameters of the maximum adsorption amount, b_1 and b_2 are the affinity constants. n_1 and n_2 are the deviations from an ideal homogeneous surface.

Based on the above model parameters of pure gas adsorption, we used the IAST model, which was proposed by Myer and Prausnitz in 1965 to predict the multi-component adsorption.[3] Analogous to Raoult's law for vapor-liquid equilibrium, the IAST assumes that the adsorbed solutions are ideal and all activity coefficients in the adsorbed phase are unity. Thus, the adsorption equilibrium between adsorbed and gas phases will lead to the following equation

$$\mathrm{P} y_i \varphi_i = x_i f_i^0(\pi) \qquad (4)$$

Where f_i^0 is the fugacity of the equilibrium gas phase corresponding to the spreading pressure π for the adsorption of pure gas i, φ_i is the gas fugacity coefficient of component i calculated by *PR* equation of state, and x_i and y_i are the molar fraction of component i at the adsorbed and bulk phases, respectively. The binary gas mixing process is carried out at constant spreading pressure π and indicated by

$$\int_0^{f_1^0} b_1^0(f_1) d\ln(f_1) = \int_0^{f_2^0} b_2^0(f_2) d\ln(f_2) \qquad (5)$$

Where the single-component adsorption amount and selectivity are further obtained from the above equation by numerical integration and root exploration. To investigate the separation of binary mixtures, the adsorption selectivity is defined by

$$S_{ij} = \frac{x_i/x_j}{y_i/y_j} \qquad (6)$$

Where the selectivity refers to the first component over the second one, and the x_i, x_j and y_i, y_j, denote the molar fractions of species i, j in the adsorbed and bulk phases, respectively.

Transient breakthrough of mixtures in fixed bed adsorbers

The methodology used is described in earlier publications. For the breakthrough simulations, the following parameter values were used: length of packed bed, L = 0.3 m; voidage of packed bed, ε = 0.4; superficial gas velocity at inlet, u = 0.04 m/s. The transient breakthrough simulation results are presented in terms of a *dimensionless* time as the x-axis, $\tau = \frac{tu}{L\varepsilon}$, defined by dividing the actual time, t, by the characteristic time, $\frac{L\varepsilon}{u}$. The y-axis is the dimensionless gas concentration, $\frac{c_i}{c_{i0}}$ at the outlet of the fixed bed adsorber.

Characterization

The scanning electron microscopy (SEM) images were taken on a JSM-6700F electron microscope operating at 5.0 kV. The elemental mapping images were taken on Energy Dispersive Spectrometer (EDS) on Oxford X-MAX 80. X-ray photoelectron spectroscopy (XPS) spectra were recorded using a Thermo ESCALAB250 spectrometer with monochromatized Al Kα excitation.

Captions

Figure S1. SEM images of AlPO-ERI (a), MgAPO-ERI (b) and CoAPO-ERI (c).

Figure S2. The elemental mapping images of AlPO-ERI (a), MgAPO-ERI (B) and CoAPO-ERI (c). Color code: blue, Al; purple, P; red, O; green, heteroatom (Mg or Co).

Figure S3. Experimental powder X-ray diffraction patterns of AlPO-ERI, MgAPO-ERI and CoAPO-ERI after calcination at 550 ^{o}C for 6 h, as compared with their simulated one.

Figure S4. XRD patterns of MgAPO-ERI (a) and CoAPO-ERI (b) after treatment by reflux of water at 120 ^{o}C for 2, 5, 10 h.

Figure S5. CO_2 adsorption of AlPO-ERI, MgAPO-ERI and CoAPO-ERI at 273 K (a), 283 K (b) and 298 K (c).

Figure S6. Fitting parameters of Henry's law for AlPO-ERI, MgAPO-ERI and CoAPO-ERI for CO_2 at 273 K (a) and 298 K (b), CH_4 at 273 K (c) and 298 K (d) and N_2 at 273 K (e).

Figure S7. IR spectra after adsorption of pyridine.

Figure S8. High-resolution XPS spectra of Co 2p.

Figure S9. CO_2/CH_4 IAST selectivity for AlPO- ERI, MgAPO-ERI and CoAPO-ERI at 298 K.

Figure S10. Virial fittings for CO_2 isotherms of AlPO-ERI (a), MgAPO-ERI (b) and CoAPO-ERI (c).

Figure S11. CO_2 (a) and CH_4 (b) gas adsorption isotherms for AlPO-ERI, MgAPO-ERI and CoAPO-ERI at 298 K.

Table S1. The molar contents of elements in AlPO-ERI, MgAPO-ERI and CoAPO-ERI.

Table S2. CO_2 adsorption amounts at 0.10 bar for AlPO-ERI, MgAPO-ERI and CoAPO-ERI (in $cm^3\ g^{-1}$).

Table S3. Reported CO_2 adsorption capacities for other aluminophosphate zeolites in comparison with CoAPO-ERI.

Table S4. Reported CO_2 adsorption selectivities and isosteric heat of adsorption for other zeolites, MOFs, modified materials.

Table S5. Fitting parameters of DSLF adsorption model for AlPO-ERI.

Table S6. Fitting parameters of DSLF adsorption model for MgAPO-ERI.

Table S7. Fitting parameters of DSLF adsorption model for CoAPO-ERI.

Table S8. CO_2 selectivities by Henry's law.

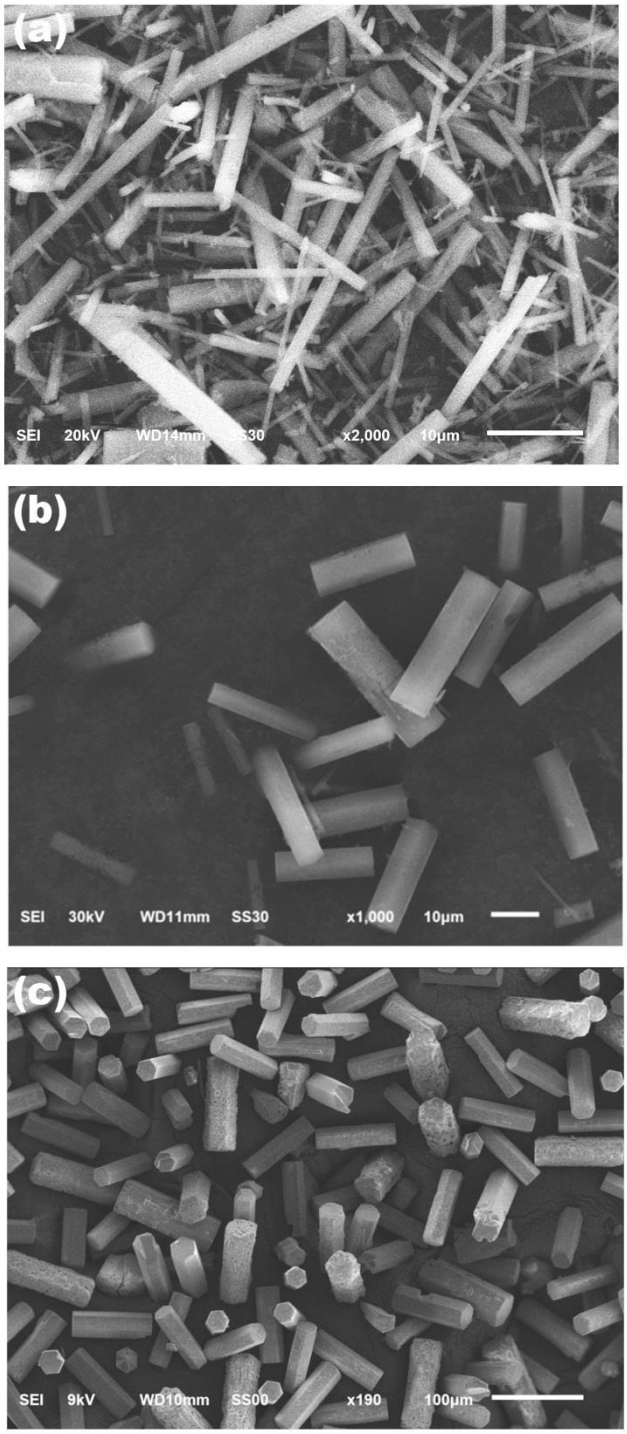

Figure S1. SEM images of AlPO-ERI (a), MgAPO-ERI (b) and CoAPO-ERI (c).

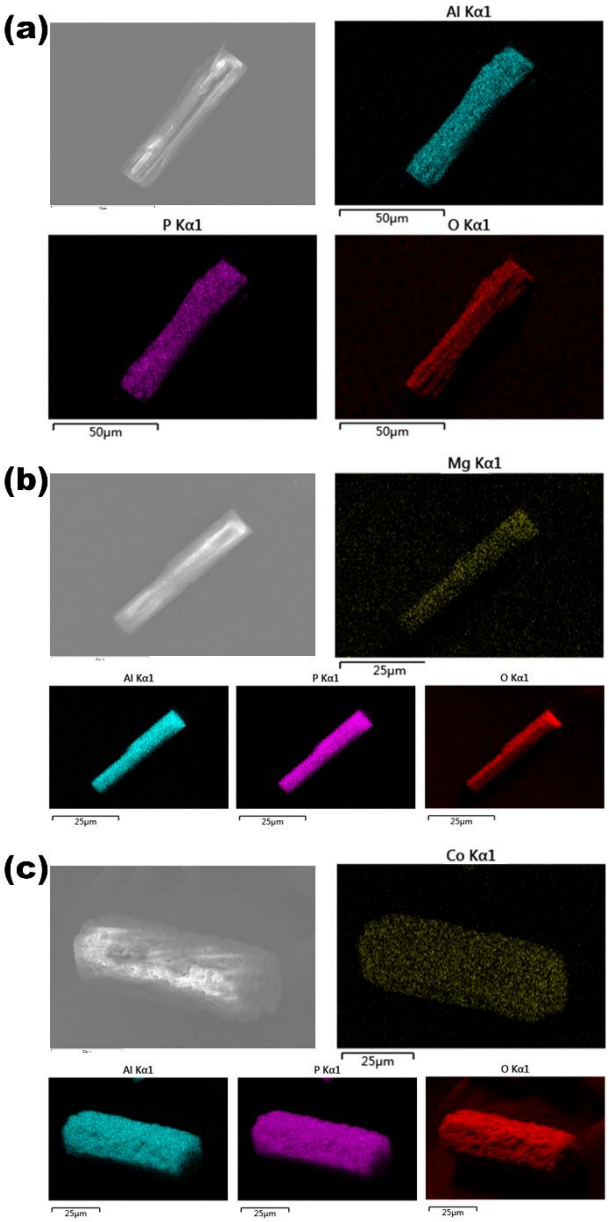

Figure S2. The elemental mapping images of AlPO-ERI (a), MgAPO-ERI (B) and CoAPO-ERI (c). Color code: blue, Al; purple, P; red, O; green, heteroatom (Mg or Co).

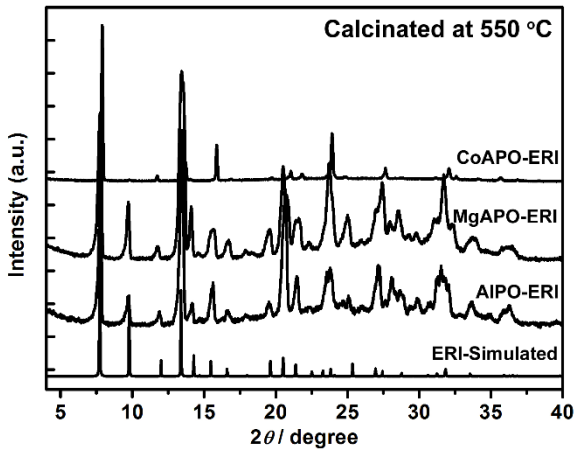

Figure S3. Experimental powder X-ray diffraction patterns of AlPO-ERI, MgAPO-ERI and CoAPO-ERI after calcination at 550 ^{o}C for 6 h, as compared with their simulated one.

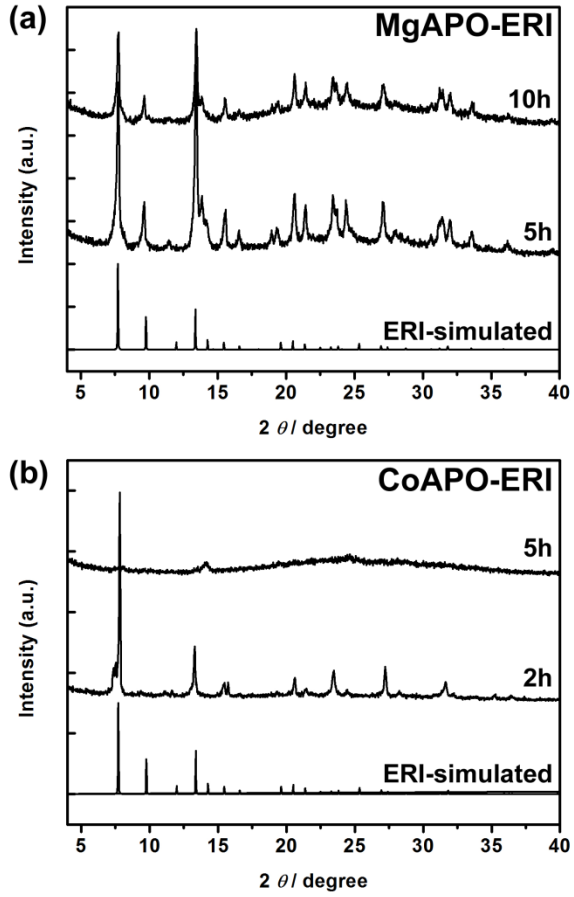

Figure S4. XRD patterns of MgAPO-ERI (a) and CoAPO-ERI (b) after treatment by reflux of water at 120 ^{o}C for 2, 5, 10 h.

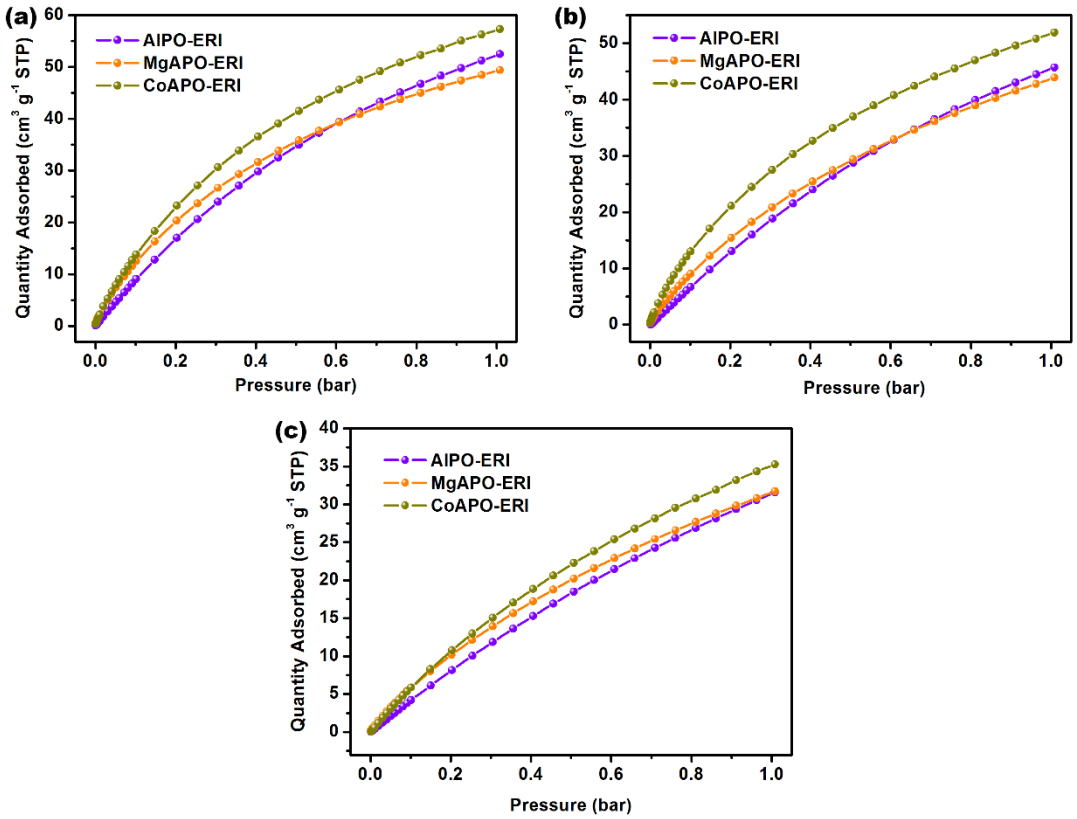

Figure S5. CO_2 adsorption of AlPO-ERI, MgAPO-ERI and CoAPO-ERI at 273 K (a), 283 K (b) and 298 K (c).

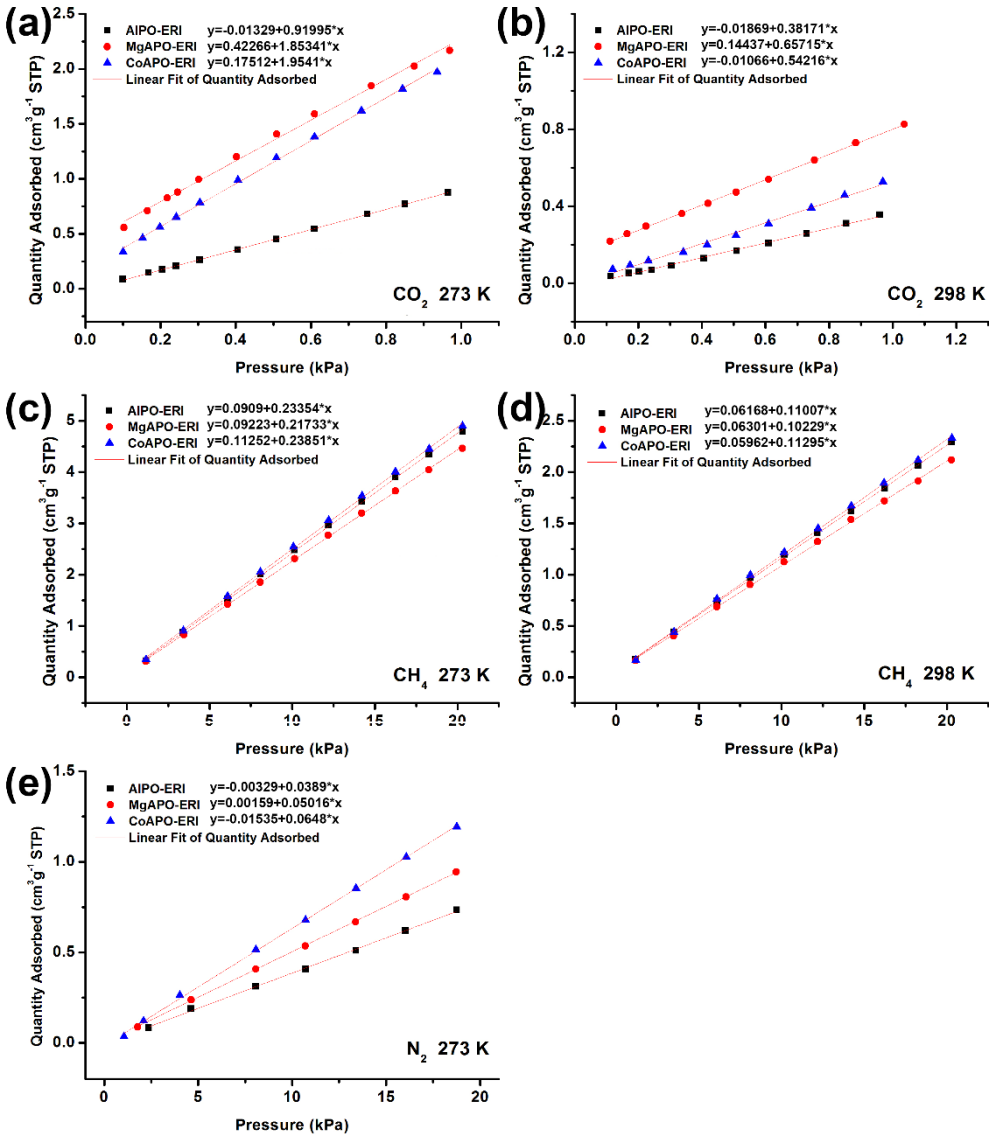

Figure S6. Fitting parameters of Henry's law for AlPO-ERI, MgAPO-ERI and CoAPO-ERI for CO_2 at 273 K (a) and 298 K (b), CH_4 at 273 K (c) and 298 K (d) and N_2 at 273 K (e).

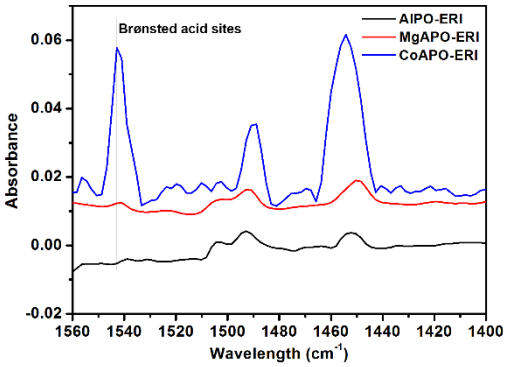

Figure S7. IR spectra after adsorption of pyridine.

(For the 8-ring zeolites, the probe molecule pyridine is big. This might be a reason for the weak signal).

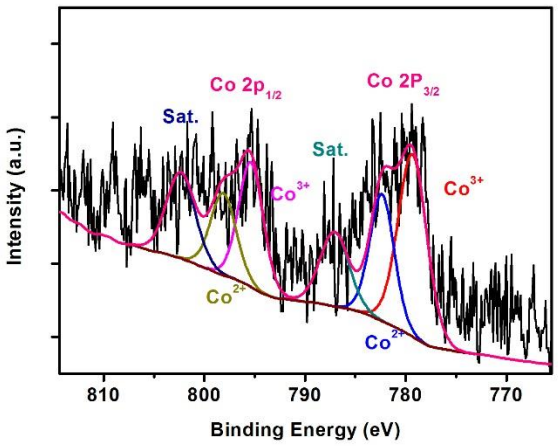

Figure S8. High-resolution XPS spectra of Co 2p.

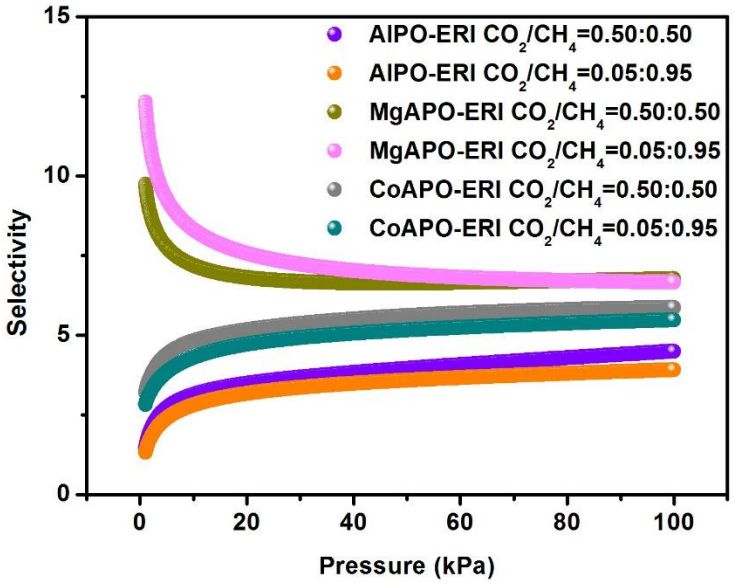

Figure S9. CO_2/CH_4 IAST selectivity for AlPO- ERI, MgAPO-ERI and CoAPO-ERI at 298 K.

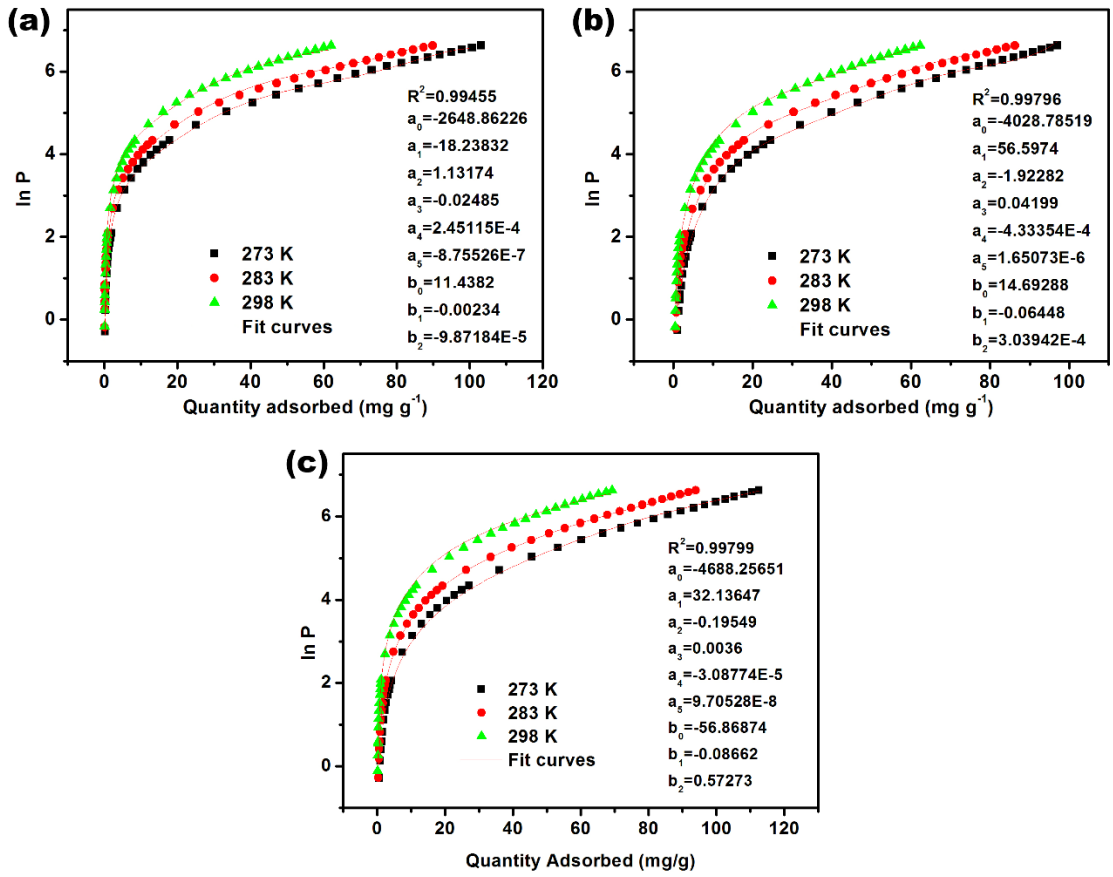

Figure S10. Virial fittings for CO_2 isotherms of AlPO-ERI (a), MgAPO-ERI (b) and CoAPO-ERI (c).

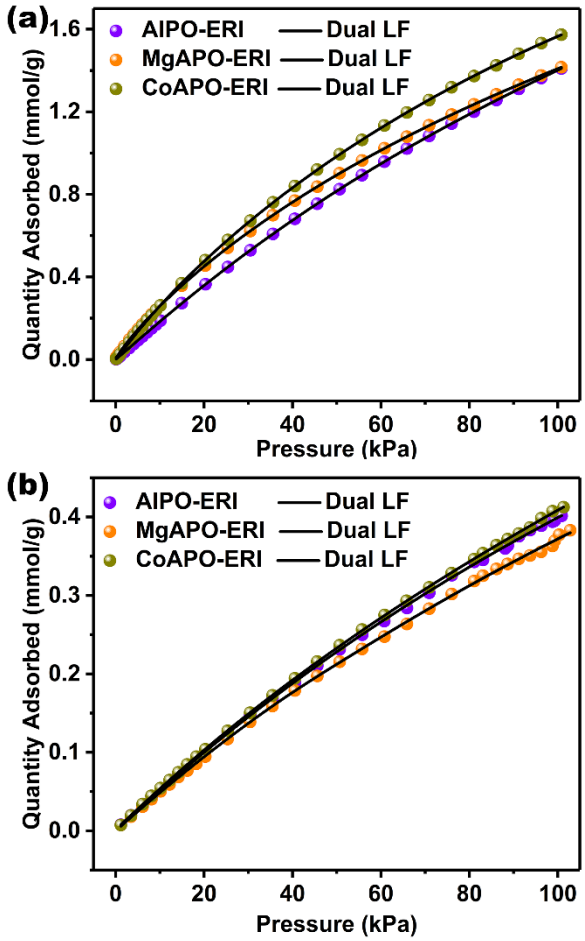

Figure S11. CO_2 (a) and CH_4 (b) gas adsorption isotherms for AlPO-ERI, MgAPO-ERI and CoAPO-ERI at 298 K

Table S1. The molar contents of elements in AlPO-ERI, MgAPO-ERI and CoAPO-ERI.

Sample	Al	P	M	(Al+M)/P	Substitution/%
AlPO-ERI	12.8	15.04	-	0.98	-
MgAPO-ERI	7.03	7.53	0.67	1.02	8.7
CoAPO-ERI	6.01	6.91	0.97	1.01	13.9

Table S2. CO_2 adsorption amounts at 0.10 bar for AlPO-ERI, MgAPO-ERI and CoAPO-ERI (in $cm^3\ g^{-1}$).

	273 K	283 K	298 K
AlPO-ERI	9.08	6.71	4.22
MgAPO-ERI	12.50	9.07	5.87
CoAPO-ERI	13.81	13.02	5.88

Table S3. Reported CO_2 adsorption capacities for other aluminophosphate zeolites in comparison with CoAPO-ERI.

Material name	**Topology**	**Condition**	**CO_2 capacity / mmol g^{-1}**	**Ref.**
CoAPO-ERI	**ERI**	273 K, 1 bar	2.6	This work
AlPO-ERI	**ERI**	273 K, 1 bar	2.3	This work
AlPO-14	**AFN**	273 K, 100 kPa	2.7	4
ULM-6-calcined	**AFN**	298 K, 101 kPa	1.89	5
JU93	**AEN**	273 K, 1 atm	1.84	6
AlPO-17	**ERI**	273 K, 100 kPa	2.5	7
AlPO-53	**AEN**	273 K, 100 kPa	1.65	
AlPO-18	**AEI**	273 K, 100 kPa	2.1	8
AlPO-17	**ERI**	273 K, 100 kPa	2.3	
AlPO-53	**AEN**	273 K, 100 kPa	1.9	
AlPO-25	**ATV**	273 K, 100 kPa	1.1	
AlPO-11	**AEL**	298 K, 100 kPa	0.8	9
H^+-CoAPO	**SBE**	298 K, 1 atm	1.2	10

Table S4. Reported CO_2 adsorption selectivities and isosteric heat of adsorption for other zeolites, MOFs, modified materials.

Material name	CO_2 capacity		CO_2/CH_4		CO_2/N_2		Q_{st}		Ref.
	Condition	Uptake / mmol g^{-1}	Condition	Selectivity	Condition	Selectivity	CO_2	CH_4	
AlPO-14	273K, 100 kPa	2.71	300 K	6.24			35.2	12.8	4
DD3R	273K, 100 kPa	1.9	298 K	7.39			32	18.8	11
SBA-15	298 K, 100 kPa	3.5	298 K	5.7	298 K	14			12
LTA	303K, 100 kPa	1.0-5.1	303 K	3.5-1270.6			21-49	17-27	13
Si-CHA	298 K, 100 kPa	0.47	298 K	4.06			21	17.1	14
MOF-5	303K, 100 kPa	1.9	298 K	1.8			14.9	5.1	15
ZIF-8	273K, 100 kPa	62.7 mg g^{-1}	303 K	2.6					16
UiO-66(Zr)-$(COOH)_2$	303K, 100 kPa	3.9			303 K, 1.0 bar CO_2:N_2=15:85	56	34.8		17
SNNU-12	273K, 1 atm	3.92	273 K, CO_2/CH_4=1:1	15.5			21.3	2.9	18

Cu-SSZ-13	298 K, 100 kPa	3.75	298 K, 0.15 bar CO_2 and 0.75 bar N_2	72.0			32.3		19
H-SSZ-13	298 K, 100 kPa	3.98	298 K, 0.15 bar CO_2 and 0.75 bar N_2	73.6			33.6		19
P-1	273 K, 1.1 bar	8.9 wt%	298 K, 1.1 bar	4	298 K, 1.1 bar	29	38.8	40.81	20
P-2	273 K, 1.1 bar	8.9 wt%	298 K, 1.1 bar	3	298 K, 1.1 bar	8	30.9	33.69	20
MCM-41	298 K, 100 kPa	30.2 mg g^{-1}	298 K, 1.0 bar, CO_2/CH_4=1:1	5.1	298 K, 1.0 bar, CO_2/N_2=2:8	11			21
K-MCM-22/15	273K, 100 kPa	69.4 cm^3 g^{-1}					41		22
cation-exchanged SBA-15	273K, 100 kPa	26.6-31.6 cm^3 g^{-1}					30-34		23

Table S5. Fitting parameters of DSLF adsorption model for AlPO-ERI.

	CO_2 at 273 K	CO_2 at 298 K	CH_4 at 273 K	CH_4 at 298 K	N_2 at 273 K
q_{m1}	4.54866	4.25719	993.55577	1.8824	0.4109
q_{m2}	0.03071	0.04625	1.49776	1.68738	2.38739
b_1	0.00897	0.00334	4.14164E-7	7.69221E-4	3.29769E-9
b_2	2.61079E-6	0.05682	0.00724	0.00306	7.47039E-4
$1/n_1$	1.02898	1.07312	1.32603	0.23337	3.71053
$1/n_2$	3.70248	1.23913	1	1	0.99063
R^2	0.99999	0.99999	0.99999	0.99986	0.99997

Table S6. Fitting parameters of DSLF adsorption model for MgAPO-ERI.

	CO_2 at 273 K	CO_2 at 298 K	CH_4 at 273 K	CH_4 at 298 K	N_2 at 273 K
q_{m1}	0.4533	4.62007	1.30763	0.90348	0.21647
q_{m2}	3.50804	1.25482	130.69686	48.89303	2.08786
b_1	0.11029	0.00605	0.00652	0.00478	7.61302E-9
b_2	0.01596	0.00806	1.56506E-5	1.98398E-5	0.00109
$1/n_1$	0.46159	0.78519	1.01137	0.98107	3.54794
$1/n_2$	0.95449	1	1	1	1
R^2	0.99999	0.99999	1.30763	0.90348	0.99999

Table S7. Fitting parameters of DSLF adsorption model for CoAPO-ERI.

	CO_2 at 273 K	CO_2 at 298 K	CH_4 at 273 K	CH_4 at 298 K	N_2 at 273 K
q_{m1}	4.31958	0.11486	90.53807	0.06194	0.09667
q_{m2}	0.53105	3.67357	1.4914	12.38541	4.84545
b_1	0.02152	0.06092	2.3667E-5	0.00139	7.72506E-21
b_2	0.00485	0.00508	0.00652	5.3235E-4	5.75107E-4
$1/n_1$	0.82737	1.23368	1.00982	1.74626	1.0719
$1/n_2$	1.44881	1.05592	1	0.87416	1
R^2	0.99999	0.99999	0.99998	0.99996	0.99970

Reference

1 Rowsell, J. L. C.; Yaghi, O. M. Effects of Functionalization, Catenation, and Variation of the Metal Oxide and Organic Linking Units on the Low-pressure Hydrogen Adsorption Properties of Metal-Organic Frameworks. *J. A. Chem. Soc.* **2006**, *128*, 1304-1315.

2 Ruthven, D. M. *Principles of Adsorption and Adsorption Processes; Wiley*: New York, **1984**.

3 Myers, A. L.; Prausnitz, J. M. Thermodynamics of Mixed-gas Adsorption. *AIChE. J.* **1965**, *11*, 121-127.

4 Zhao, X.-X.; Xu, X.-L.; Sun, L.-B.; Zhang, L.-L.; Liu, X.-Q. Adsorption Behavior of Carbon Dioxide and Methane on AlPO4-14: A Neutral Molecular Sieve. *Energy Fuels* **2009**, *23*, 1534-1538.

5 Wang, D.; Xu, S.; Yang, M.; Chu, Y.; Tian, P.; Liu, Z. Microporous Aluminophosphate ULM-6: Synthesis, NMR Assignment, and Its Transformation to $AlPO_4$-14 Molecular Sieve. *J. Phys. Chem. C* **2016**, *120*, 11854-11863.

6 Wang, Y.; Sun, Y.; Mu, Y.; Zhang, C.; Li, J.; Yu, J. Organotemplate-free Hydrothermal Synthesis of An Aluminophosphate Molecular Sieve with AEN Zeotype Topology and Properties of Its Derivatives. *Chem. Commun.* **2014**, *50*, 15400-15403.

7 Akhtar, F.; Keshavarzi, N.; Shkarova, D.; Cheung, O.; Hedin, N.; Bergström, L. Aluminophosphate Monoliths with High CO_2-over-N_2 Selectivity and CO_2 Capture Capacity *RSC Adv.* **2014**, *4*, 55877-55883.

8 Liu, Q.; Cheung, N. C. O.; Garcia-bennett, A. E.; Hedin, N. Aluminophosphates for CO_2 Separation. *ChemSusChem* **2011**, *4*, 91–97.

9 Delgado, J. A.; Águeda, V. I.; Uguina, M. A.; Sotelo, J. L.; Fernández, P. Adsorption and Diffusion of Nitrogen, Methane and Carbon Dioxide in Aluminophosphate Molecular Sieve $AlPO_4$-11. *Adsorption* **2013**, *19*, 407-422.

10 Hernandez-Maldonado, A. J.; Cabanzo-Olarte, A. C.; Maldonado-Aviles, S. M. Modification of a Cobalt-aluminophosphate (Co/Al∼1) with a Multidimensional Pore System via Coupled Partial Detemplation and Solid State Ion Exchange with Alkali Metals for the Adsorption of Light Gases. *Microporous Mesoporous Mater.* **2012**, *161*, 148-153.

11 Himeno, S.; Tomita, T.; Suzuki, K.; Yoshida, S. Characterization and Selectivity for Methane and Carbon Dioxide Adsorption on the All-silica DD3R Zeolite. *Microporous Mesoporous Mater.* **2007**, *98*, 62-69.

12 Liu, X.; Li, J.; Zhou, L.; Huang, D.; Zhou, Y. Adsorption of CO_2, CH_4 and N_2 on Ordered Mesoporous Silica Molecular Sieve. *Chem. Phys. Lett.* **2005**, *415*, 198-201.

13 Palomino, M.; Corma, A.; Rey, F.; Valencia, S. New Insights on CO_2-Methane Separation using LTA Zeolites with Different Si/Al Ratios and a First Comparison with MOFs. *Langmuir* **2009**, *26*, 1910-1917.

14 Maghsoudi, H.; Soltanieh, M.; Bozorgzadeh, H.; Mohamadalizadeh, A. Adsorption Isotherms and Ideal Selectivities of Hydrogen Sulfide and Carbon Dioxide over Methane for the Si-CHA Zeolite: Comparison of Carbon Dioxide and Methane Adsorption with the All-silica DD3R Zeolite. *Adsorption* **2013**, *19*, 1045-1053.

15 Bastin, L.; Bárcia, P. S.; Hurtado, E. J.; Silva, J. A. C.; Rodrigues, A. E.; Chen, B. A Microporous Metal-Organic Framework for Separation of CO_2/N_2 and CO_2/CH_4 by Fixed-bed Adsorption. *J. Phys. Chem. C* **2008**, *112*, 1575-1581.

16 Huang, H.; Zhang, W.; Liu, D.; Liu, B.; Chen, G.; Zhong, C. Effect of Temperature on Gas Adsorption and Separation in ZIF-8: A Combined Experimental and Molecular Simulation Study. *Chem. Eng. Sci.* **2011**, *66*, 6297-6305.

17 Yang, Q.; Vaesen, S.; Ragon, F.; Wiersum, A. D.; Wu, D.; Lago, A.; Devic, T.; Martineau, C.; Taulelle, F.; Llewellyn, P, L.; Jobic, H.; Zhong, C.; Serre, C.; Weireld, G. D.; Maurin, G. A Water Stable Metal–Organic Framework with Optimal Features for CO_2 Capture. *Angew. Chem. Int. Ed*. **2013**, *52*, 10316-10320.

18 Zhang, J.-W.; Hu, M.-C.; Li, S.-N.; Jiang, Y.-C.; Zhai, Q.-G. Design of Highly Connected Cd-Tetrazolate-Dicarboxylate Frameworks with Enhanced CO_2/CH_4 and C2 Hydrocarbons/CH_4 Separation Performance. *Crystal Growth & Design* **2016**, 16, 6430-6435.

19 Hudson, M. R.; Queen, W. L.; Mason, J. A.; Fickel, D. W.; Lobo, R. F.; Brown, C. M. Unconventional, Highly Selective CO_2 Adsorption in Zeolite SSZ-13. *J. Am. Chem. Soc*. **2012**, *134*, 1970-1973.

20 Qiao, S.; Du, Z.; Yang, R. Design and Synthesis of Novel Carbazole-spacer-carbazole Type Conjugated Microporous Networks for Gas Storage and Separation. *J. Mater. Chem. A*. **2014**, *2*, 1877-1885.

21 Belmabkhot, Y.; Sayari, A. Adsorption of CO_2 from Dry Gases on MCM-41 Silica at Ambient Temperature and High Pressure. 2: Adsorption of CO_2/N_2, CO_2/CH_4 and CO_2/H_2 Binary Mixtures. *Chem. Eng. Sci*. **2009**, *64*, 3729-3735.

22 Zukal, A.; Pawlesa, J.; Čejka, J. Isosteric Heats of Adsorption of Carbon Dioxide on Zeolite MCM-22 Modified by Alkali Metal Cations. *Adsorption* **2009**, *15*, 264-270.

23 Zukal, A.; Mayerová, J.; Čejka, J. Alkali Metal Cation Doped Al-SBA-15 for Carbon Dioxide Adsorption. *Phys. Chem. Chem. Phys*. **2010**, *12*, 5240-5247.